Source parameters of the 1 October 1995 Dinar (Turkey) earthquake from SAR interferometry and seismic bodywave modelling

T.J. Wright [a,⋆], B.E. Parsons [a], J.A. Jackson [b], M. Haynes [c], E.J. Fielding [a,d], P.C. England [a] and P.J. Clarke [a,e]

[a] *Department of Earth Sciences, University of Oxford, Parks Rd, Oxford OX1 3PR, U.K.*

[b] *Department of Earth Sciences, University of Cambridge, Downing Street, Cambridge, UK.*

[c] *Nigel Press Associates, Crockham Park, Edenbridge, Kent, TN8 6SR, UK.*

[d] *Also at Jet Propulsion Laboratory, 4800 Oak Grove Drive, Pasadena, CA, 91109, USA.*

[e] *Now at Department of Geomatics, University of Newcastle, Newcastle, NE1 7RU, UK.*

Abstract

The 1 October 1995, M_s = 6.1 Dinar earthquake ruptured a 10km section of the NW-SE Dinar-Çivril fault. Discrepancies exist between the published source parameters, with seismic moments in disagreement by over a factor of two. We use both SAR interferometry and seismic bodywave modelling to determine earthquake source parameters. An interferogram generated from ERS-1/2 SAR imagery spanning the event and separated by 5 months is used to derive source parameters by a downhill simplex inversion with multiple Monte-Carlo restarts. Initially we model the line-of-sight displacements using a uniform slip on a rectangular dislocation in elastic half space. The resultant model fault plane agrees in strike and location with the observed surface break, but significant residuals exist in the line-of-sight deformation field resulting in a r.m.s. residual of half a fringe (15mm). The residuals are reduced by segmenting the fault plane, allowing depths and magnitude of slip to vary spatially. Our best fitting solution, with a r.m.s. misfit of a quarter of a fringe (7mm), reveals two distinct areas of slip on the fault plane: a main rupture slipping by 1.25 m between depths of 1 and 7km, becoming deeper to the SE and matching the observed surface rupture, and 0.73 m of slip to the NW on an along-strike continuation of the same fault plane, but between depths of 5 and 15 km and not associated with a surface break. The total geodetic moment (3.9×10^{18}Nm) is nearly twice as large as published seismic moments based on the inversion of P–waveforms. We use SH–waveforms in addition to the P–waves used previously to determine a seismic source mechanism. SH–waves constrain the depth to be shallower than solutions based on P–waves alone, agreeing with the depths from the interferometric inversion and resulting in a larger moment, although our seismic moment is still 25% smaller than the total geodetic moment.

⋆ Corresponding Author. Tel.: +44 (0)1865 272016; E-mail: tim.wright@earth.ox.ac.uk

1 Introduction

Southwest Turkey forms part of the highly seismically-active Aegean extensional domain [1,2], characterised by N-S distributed extension (Figure 1). GPS crustal velocity measurements [3] indicate a regional extension rate of $14 \pm 5 \mathrm{mmyr}^{-1}$. In south-west Anatolia the tectionic setting is more complex, with the Isparta Angle representing the intersection of the Hellenic and Cyprus arcs [4]. Both NE-SW and NW-SE faults are present, with the former appearing to be the dominant system. The NE-SW Fethiye-Burdur fault zone, characterised by left-lateral slip with an element of normal faulting [5], is the north-eastern extension of the Pliny-Strabo fault zone (part of the Hellenic arc) and has been the site of a number of large earthquakes this century. At its north-eastern end, the Fethiye-Burdur fault zone is limited by a NW-SE striking fault, the Dinar-Çivril fault.

The 1 October 1995, $M_s = 6.1$ Dinar earthquake ruptured a section of the Dinar-Çivril fault which is characterised by a 60km scarp with up to 1500m of relief to the NE, although there is only approximately half this relief at the rupture location. The earthquake created a 10km continuous surface rupture running along the base of the scarp with a maximum vertical offset of 25-30cm, tailing off to around 15cm at the SE [6] . Landsat TM imagery has been used in conjunction with a digital elevation model derived in this study to give a perspective view of the Dinar-Çivril fault (Figure 2). The topography has a classic tilted block geometry with a steep scarp against the fault plane and gently tilted backslope. The earthquake caused extensive damage to the town of Dinar and killed 92 inhabitants.

There are discrepancies between published seismic source parameters (Table 1) with seismic moments in disagreement by over a factor of two. The scaling of seismic moment M_0 with fault length L and width W is fundamentally important in seismology and has been studied by many authors, e.g.[7,8]. Accurate knowledge of moment release is also vital for seismic hazard analysis [9]. In this study we have used SAR interferometry to separately determine fault length, width and slip, hence M_0, independently of seismology and without additional information from aftershock distributions. Our geodetic solution for the source parameters of the Dinar earthquake constrains the seismic moment to be larger than previous solutions based on P–wave modelling [6,10]. We investigated the reasons for this using SH–waveforms jointly with the P–waves used previously.

2 Source parameters from P– and SH– bodywave modelling

A number of published seismic mechanisms exist (Table 1), notably those determined from inversion of P–waves by Eyidŏgan and Barka [6] and Pinar [10]. These solutions differ from each other and from the Harvard CMT solution whose seismic moment is more than twice as large. We sought a source mechanism using SH–body-wave inversion in addition to the P–waves used previously. The method and approach used is described in detail elsewhere [11,12,2]. We used the MT5 software [13] to create a best fit seismic inversion solution (Table 1, Figure 3). [JAMES: More detail needed on – starting solution ? Assumptions ? Crustal structure ? Location?]

Eyidŏgan and Barka, and Pinar discount SH–waves because of noise levels. However, we found plenty of stations whose SH–waves are clear, with those at the same position on the focal sphere having very similar shapes (e.g. AAK, LSA, NIL, and CHTO; or COL and KBS; or SSPA and SJG), so we are confident these SH signals are real. The fit to SH–waves is bad at a few stations very close to an SH nodal plane (e.g. ERM, HIA, BRVK) as in those cases the waveforms are extremely sensitive to very small changes in the nodal planes. At stations away from the nodal planes, and at a wide variety of azimuths, the fit to the SH waveforms is good (e.g. AAK, LSA, NIL, and CHTO; LBTB; SSPA and SJG; KBS, and COL).

The principal feature of the source time function is a double pulse, corresponding to two bursts of moment release, or sub-events, with the larger second event starting about 5 seconds after the first. This is a feature of the Eyidŏgan and Barka and Pinar solutions too, although we constrain both events to lie on the same fault plane. Our seismic moment is 50% larger than those determined from P–waves alone, although it is still smaller than the Harvard CMT solution. The difference, between the moment constrained by P–waveforms alone and that determined from both P– and SH–wave modelling, probably arises because of a strong trade-off between source depth and length of the source time function resulting in larger seismic moments for events at shallower depths. Figure 4 shows waveforms recorded at 6 stations from different parts of the focal sphere. Row A is our best fitting solution and row B is the best fitting solution with depth constrained to 10km. The deeper source is fitted by a shorter source time function with a moment which is approximately half the size of the best fitting solution. Although the fit of the P–waves does not significantly change with increased depth, the SH–waves are modelled better by a shallow source thus requiring our moment to be larger than the published deeper sources.

The shape of the source time function (Figure 4, row A) contains a tail at the end of the second (main) sub-event giving the time function a total duration

of 20 seconds. If we limit the time function to 14 seconds duration, removing the tail, the resulting inversion (Figure 4, row C) gives a solution whose fit to the waveforms is not significantly worse than in line 1, and whose source parameters are also negligibly different except for the moment, which has reduced from 3.1×10^{18} to 2.7×10^{18}Nm. Thus about 10-15% of the moment in our best-fitting solution is contained in the tail of the time function, which is poorly resolved. This gives an indication of the likely error in the moment, constraining it to $3.0\pm0.3 \times 10^{18}$Nm.

The published solutions state that the second sub-event is NW of the first, because the time delay between the two pulses in the P–waveforms apparently varies with azimuth. This critically depends on the onset time chosen for the P–waveforms: in our inversion this is fixed to the arrival time read on the (relatively) high-frequency broad band records at all stations. If source directivity is significant, it will result in a compression of the time function and waveforms in the direction of rupture propagation and elongation of them in the opposite direction. There is a suggestion of this in the P–waveforms at some locations (e.g. MSEY and SJG). Tests using a source propagating NW (315^o) at 2 km s^{-1} (Figure 4, row D) improved the P–wave fit at several, but not all, stations but the fit to the SH–waves worsens. We conclude that we cannot reliably resolve rupture propagation using the P and SH data.

3 SAR Interferometry

Studies of previous earthquakes, the Landers event in particular, have established SAR interferometry as a valuable technique for studying ground displacements caused by earthquakes [15–18]. Images acquired before and after an event in which ground displacements have occurred can be used to generate an interferogram giving measurements with subcentimetric precision over a wide area with a high spatial sampling rate.

Coseismic movements from the Dinar Earthquake were measured using ERS SAR images spanning the event (Table 2, pair A) with a 5 month temporal separation and a 1165 m altitude of ambiguity (h_a); i.e. topographic relief of 1165 m produces a single fringe. We used the PulSAR SAR processing software and the DERAin interferometric software, developed by the Defence Evaluation Research Agency, to create the coseismic interferogram. The orbital parameters were updated using precise orbits from the German Processing and Archiving Facility (D-PAF).

The small topographic contribution to the net fringes was removed using a high resolution Digital Elevation Model (DEM) constructed from an ERS tandem pair (table 2, pair B), using the ROI_pac software at JPL. The unwrapped

phase differences [19] were converted to elevations [20] with the effective baseline and phase constant being determined by comparing the unwrapped phase with a medium resolution DEM for the Dinar area (Figure 2).

The corrected coseismic interferogram (Figure 5) shows 21 fringes in the hanging wall of the fault indicating a maximum line-of-sight downthrow displacement of 0.59m. The hanging-wall fringe pattern indicates a slightly asymmetrical deformation with the maximum displacement towards the NW end of the observed surface rupture but about 2km away from it, forming a 'bull's eye' pattern. At greater distances from the surface rupture fringes run sub-parallel to the strike direction, with fringes widening slightly to the NW before curving sharply inwards towards the ground break. Only two upthrown fringes (5.8 cm) appear in the footwall of the fault after the topographic correction. Coherence in the interferogram is strongly correlated to surface cover with high coherence over the basal conglomerates in the footwall but low coherence over the agricultural flood plain of the Menederes river.

In addition to the fringes resulting directly from the earthquake there are two localised high gradient fringe patterns (S_1, S_2). S_1 lies on the steep mountainside and S_2 lies at the base of the slope on alluvial fan deposits. Without visiting these locations it is impossible to determine what has caused the displacements but the most likely explanation is some form of land-sliding, probably triggered by the earthquake.

4 Interferometric Determination of Source Parameters

We digitised discrete line-of-sight displacements at 753 locations along identifiable fringe boundaries (where phase = 0 or 2π; Figure 6). The displacement at each point was determined relative to a nominal zero displacement fringe away from the influence of the earthquake. Initially, the event was modelled by assuming the surface deformation was equivalent to that caused by a uniform slip on a single rectangular dislocation in elastic half-space [21].

We adopt a hybrid Monte-Carlo, downhill simplex inversion technique [22,23] to calculate a best fitting model to the fringe pattern. The downhill simplex method [24,25] finds minima in the misfit between observed and model displacements. To overcome the problem of local minima, we used a Monte-Carlo approach, starting the inversion 1000 times with randomly chosen starting parameters, the lowest minima being retained as the final solution. No constraint was used in the inversion with 10 parameters in all being determined for the single dislocation solution – strike, dip, rake, slip, latitude and longitude, length of scarp, minimum and maximum depth, and a line-of-sight offset to allow for an incorrect assignment of the zero fringe.

In order to ensure that certain parameters remained positive, or within given bounds, the inversion procedure makes use of auxilliary parameters. For example, the length of the fault L is related to a parameter λ by $L = e^{\lambda}$. In the downhill simplex inversion, λ is allowed values in the range $\pm\infty$; L is automatically constrained to satisfy $0 < L < \infty$. Also, the depth of the top of the fault d was constrained to lie in the range $0 < d < d_{max}$ by allowing the downhill simplex inversion to work with parameter δ in the range $\pm\infty$, where

$$d = \frac{d_{max}}{\pi}(\frac{\pi}{2} + \tan^{-1}\delta).$$

We assigned a value of 25 km to d_{max} in order to loosely constrain the fault to lie in the seismogenic upper crust. The height of the fault was constrained in a similar way.

The source parameters constrained by our initial SAR inversion (Table 3) were used to create a model interferogram (Figure 7a). The model explains the bulk of the deformation observed in the interferogram with the maximum displacement in approximately the same location and of the same magnitude, and fringes sub-parallel to the strike direction. The root mean square misfit (15 mm.) corresponds to half a fringe (quarter of the radar wavelength). The surface projection of the fault plane predicted by the inversion matches surface observations of ground ruptures [6] almost exactly for location and size.

Despite this good fit over the majority of the fringe pattern, two areas in particular are not well modelled. Firstly, the shape of the maximum in the model interferogram does not match the 'bull's eye' pattern of the real interferogram. The maximum in the model is much more elongate, resulting in several residual fringes (Figure 7b, R_1). Also, the fringes in the NW corner of the model interferogram do not have the observed tightness of curvature, with the far field pattern in the model having smoother, more gradual changes. Again this results in a significant residual (Figure 7b, R_2). It is impossible to remove either of these residuals using our single fault model whilst maintaining a good fit to the remainder of the deformation pattern.

To increase the quality of the fit we tried two approaches, each of which increases the complexity of the model, either by adding additional fault planes or by subdividing the plane of the single fault solution. With 9 inversion parameters per fault, solutions with multiple fault segments required some restrictions to avoid overfitting the data. Hence segment locations, lengths and strikes were fixed and we inverted for a single value of dip and rake applying to all segments. Segment locations were constrained to the position of our single fault plane model or its along-strike continuation.

By subdividing the single fault solution into 3 separate segments, inverting for slip and depths for each, we are able to model the 'bull's eye' and remove residual R_1. The feature is matched by terminating the fault closer to the

surface at the NW end of the rupture than the SE, with approximately the same slip on each segment. Because the improvement in fit resulted from variations in depth along these segments, we were able to invert for just a single slip. We also attempted inversions with additional fault segments as continuations to the single fault solution. A single continuation of the fault to the NW with slip below 5 km was found to improve the fit at R_2. Other configurations with along-strike continuations in different locations, including continuations to the SE, did not influence the fit to the interferogram data.

Our best fitting solution was generated from a four segment constrained inversion, three equal length segments lying on the fault plane from the single fault solution and an along-strike continuation to the NW. Thirteen parameters were inverted for in all: a rake and dip applying to all segments, slip of main section, slip on continuation, 4 segment minimum and maximum depths, and a line-of-sight offset.

The inversion results (Table 3; Figure 8) show a very good match to the input interferogram, with all the major features of the original reproduced. The r.m.s. residual has been reduced from 15 mm to 7 mm, or a quarter of a fringe, not significantly larger than a typical level of atmospheric noise [26,27]. Our solution implies that there are two separate areas of slip on the fault plane: a main rupture slipping by 1.25 m between depths of 1 and 7 km, matching the location of the observed surface rupture, and slip of 0.73 m to the NW on an along-strike continuation of same fault plane, but between depths of 5 and 15 km and not associated with a surface rupture. The time interval between SAR acquisitions means that our solution cannot give us information on the timing of slip in these different areas.

5 Discussion

All the source parameter solutions, whether seismic or interferometric, broadly agree on the orientation of the fault plane of the Dinar earthquake - striking at around 135^o and dipping at approximately 45^o with an almost purely normal slip. There is more disagreement over seismic moment with estimates from 2×10^{18}[6] to 4.7×10^{18}Nm [Harvard CMT]. P– and SH–waveform modelling shows that the estimated depth of the earthquake is crucial in determining the moment, with the best-fitting seismic solutions having a larger moment for shallower depths. The interferometric inversion suggests that most of the slip was shallow, above depths of 7 km. When SH–waves are used in the inversion for source parameters, the depth of the earthquake is constrained to be shallower than solutions based on P–waves alone, agreeing with the depths from the interferometric inversion and resulting in a larger moment. However, the total geodetic moment is still 25% larger (3.9×10^{18}Nm) than the seismic

moment (3.1×10^{18}Nm).

The geodetic solution is derived from SAR imagery spanning a 5 month period and therefore includes all foreshocks, aftershocks and any post-seismic displacements in the 3 months after the event. Aftershock locations and magnitudes are available from the Kandilli Observatory and Earthquake Research Institute (KOERI) network, a regional network for Turkey. Figure 9 shows the foreshock and aftershocks ($M_d >= 4$) around the Dinar fault which occurred between the dates of image acquisition, in fact all of this activity occurred within two weeks of the mainshock. Although the accuracy of the locations is not known, the activity of these events is confined to approximately the same area as our geodetic model solution. The more widespread distribution noted by Pinar [10], which included numerous events between 15 and 25km depth, is not found when observing the larger shocks ($M_d >= 4$) . The total moment of the foreshock and aftershock activity is sufficient to account for the discrepancy between our geodetic and seismic solutions.

[James: what about CMT ????]

Our model terminates a minimum of 1 km below ground despite a surface rupture being observed. We also found there to have been over a metre of slip on the fault whereas no more than 30 cm of offset was observed at the surface. We model the event using uniform slip on rectangular fault planes. If the top of the faults are constrained to break the surface, the maximum displacement in the resultant fringe pattern moves from 2 km away from the surface rupture to a position alongside it. The evidence suggests that the fault has non-uniform slip with respect to depth with the average slip over the majority of the fault plane being over a metre. Our approach was to use the simplest possible model to explain the interferogram. Constraining the model to a uniform slip on each fault plane requires the faults to terminate below ground, not allowing for a tailing off of slip towards the surface.

Despite a high coherence in the footwall of the fault, we do not match the displacements well there, with the model predicting less deformation than was actually the case. Again this could result from afterslip and post-seismic deformations in the 3 months after the event. Atmospheric effects such as the altitude dependence of the propagation delay of electromagnetic waves in the lower troposphere [28] could also result in complications in the footwall fringe pattern, but these are unquantifiable without additional meteorological data. It is unlikely that the misfit is caused by an error in the DEM because we would require errors of over 1000 m to produce a single fringe.

This study has demonstrated the uncertainties that can exist in the determination of seismic moment and the value of using all sources of information to address the problem. Source parameters of shallow earthquakes determined

by bodywave modelling can underestimate the moment by overestimating the depth of the event. The moment determined using P– and SH–waves is nearly twice as large as previously published mechanisms based on P–wave modelling, though still slightly less than that obtained from SAR interferometry. The inversion of line-of-sight ground displacements enables separate estimates of slip and the dimensions of the fault to be made. The shape of the fringe pattern, to the extent that the coherence of the interferogram allows this to be defined, also contains information about variations in slip and its depth distribution. Future methods should be able to improve on the simple methods used here of representing non-uniform slip.

6 Acknowledgements

We gratefully acknowledge the research studentship awarded to TJW by the Natural Environment Research Council in association with Nigel Press Associates. We thank Ren Capes, Geoff Lawrence and Nigel Press for encouraging us to undertake this study, and Nigel Press Associates for providing the ERS SAR data. We also thank Goran Ekstrom for discussing with us his unpublished source modelling of the Dinar earthquake.

References

[1] D. McKenzie, Active Tectonics of the Alpine-Himalayan belt: the Aegean Sea and surrounding regions, Geophys. J. R. Astron. Soc. 55 (1978) 217–254.

[2] T. Taymaz, J. Jackson, D. McKenzie, Active tectonics of the north and central Aegean Sea, Geophys. J. Int. 106 (1991) 433-490.

[3] R. Reilinger, S.C. McClusky, M.B. Oral, R.W. King, M.N. Toksoz, A.A. Barka, I. Kinik, O. Lenk, I. Sanli, Global Positioning System measurements of present-day crustal movements in the Arabia–Africa–Eurasia plate collision zone, J. Geophys. Res. 102 (1997) 9,983–9,999.

[4] A. Barka, R. Reilinger, Active Tectonics of the Eastern Mediterranean: Deduced from GPS, Neotectonic and Seismicity Data, Annali di Geofisica XL (1997) 587–610,

[5] S. Price, B. Scott, Fault-block rotations at the edge of a zone of continental extension; southwest Turkey J. Strucy. Geol. 16(3) (1994) 381–392.

[6] H. Eyidŏgan, A. Barka, The 1 October 1995 Dinar Earthquake, SW Turkey, Terra Motae 8 (1996) 479–485.

[7] C.H. Scholtz, A reappraisal of large earthquake faulting, Bull. Seismol. Soc. Am. 84(1) (1994) 215–218.

[8] G. Pegler, S. Das, Analysis of the relationship between seismic moment and fault length for large crustal strike-slip earthquakes between 1977-92, Geophys. Res. Lett. 23(9) (1996) 905–908.

[9] R. Davies, P. England, B. Parsons, H. Billiris, D. Paradissis, G. Veis, Geodetic strain of Greece in the interval 1892-1992. J. Geophys. Res. 102 (1997) 24571–24588.

[10] A. Pinar, Source inversion of the October 1, 1995, Dinar earthquake (M_s = 6.1): a rupture model with implications for seismotectonics in SW Turkey, Tectonophysics 292 (1998) 255–266.

[11] J. Nabalek, Determination of earthquake source parameters from the inversion of body waves, Ph.D. thesis, Massachusetts Institute of Technology, 1984.

[12] R. McCaffrey, J. Nabalek, Earthquakes, gravity and the origin of the Bali basin: and example of a nascent continental fold-and-thrust belt, J. Geophys. Res. 92 (1987) 441–460.

[13] P. Zwick, R. McCaffrey, G. Abers, MT5 Program, IASPEI Software Library 4 (1995). JAMES: IS THIS REFERENCE CORRECT ??

[14] F. Şaroglu, Ö. Emre, İ. Kuşçu, Active Fault Map of Turkey, General Directorate of Mineral Research and Exploration (MTA), Eskişehir Yolu, 06520,Ankara,Turkey, 1992.

[15] D. Massonnet , M. Rossi , C. Carmona , F. Adragna , G. Peltzer , K. Fiegl , T. Rabaute, The displacement field of the Landers earthquake mapped by radar interferometry, Nature, 364 (1993) 138–142.

[16] D. Massonnet, K.L. Feigl, Discrimination of geophysical phenomena in satellite radar interferograms, Geophys. Res. Lett. 22(12) (1995) 1,537–1,540.

[17] B. Meyer, R. Armijo, J.B. de Chabalier, C. Delacourt, J.C. Ruegg, J. Acache, P. Briole, D. Papanastassiou, The 1995 Grevena (Northern Greece) Earthquake: Fault Model Constrained with Tectonic Observations and SAR Interferometry, Geophys. Res. Lett. 23(19) (1996) 2,677–2,680.

[18] B. Hernandez, F. Cotton, M. Campillo, D. Massonnet, A Comparison between short term (co-seismic) and long term (one year) slip for the Landers earthquake: Measurements from strong motion and SAR interferometry, Geophys. Res. Lett. 22(18) (1995) 2,517–2,520.

[19] R.M. Goldstein, H.A. Zebker, C.L. Werner, Satellite radar interferometry: Two-dimensional phase unwrapping, Radio Science 23(4) (1988) 713–720.

[20] H.A. Zebker, C. Werner, P.A. Rosen, S. Hensley, Accuracy of topographic maps derived from ERS-1 interferometric radar, IEEE Trans. on Geoscience and Remote Sensing, 32(4) (1994) 823–836.

[21] Y. Okada, Surface Deformation due to Shear and Tensile Faults in a Half-space, Bull. Seismol. Soc. Am. 75(4) (1985) 1,135–1,154.

[22] P.J. Clarke, D. Paradissis, P. Briole, P.C. England, B.E. Parsons, H. Billiris, G. Veis, J.-C. Ruegg, Geodetic Investigation of the 13 May 1995 Kozani – Grevena (Greece) Earthquake, Geophys. Res. Lett. 24(6) (1997) 707–710.

[23] P. Clarke, Tectonic Motions and Earthquake Deformation in Greece from GPS Measurements, D.Phil. thesis, University of Oxford, 1996, 274 pp.

[24] J.A. Nelder, R. Mead, A Simplex Method for Function Minimisation, Computer Journal, 7 (1965) 308–313.

[25] W.H. Press, S.A. Teukolsky, W.T. Vetterling, B.P. Flannery, Numerical Recipes in C: The Art of Scientific Computing, 2nd Edition, Cambridge University Press, Cambridge, U.K., 1992, 994pp.

[26] E.J. Fielding, R.G. Blom, R.M. Goldstein, Rapid subsidence over oil fields measured by SAR interferometry, Geophys. Res. Lett. 25(17) (1998) 3215–3218.

[27] R. Goldstein, Atmospheric Limitations to repeat-track radar interferometry, Geophys. Res. Lett. 22(18) (1995) 2,517–2,520.

[28] C. Delacourt, P. Briole, J. Achache, Tropospheric corrections of SAR interferograms with strong topography. Application to Etna, Geophys. Res. Lett. 25(15) (1998) 2849–2852.

Table 1. Source parameters of the 1 October 1995 Dinar Earthquake from seismology .

	Scarp Lat,Lon	M_0 / N m	Strike	Dip	Rake	Depth	No. of waveforms
Harvard CMT	38.06^o, 29.68^o	4.7×10^{18}	125^o	30^o	267^o	15 km	—
Eyidŏgan and Barka[6]							
1^{st} sub-event	38.10^o, 30.175^o [b]	0.38×10^{18}	135^o (fixed)	40^o	255^o	8 km	10[c]
2^{nd} sub-event		1.64×10^{18}	135^o (fixed)	62^o	221^o	12 km	
Pinar[10]							
1^{st} sub-event	38.09^o, 30.15^o	0.5×10^{18}	121^o	34^o	261^o	10 km	16[c]
2^{nd} sub-event		1.6×10^{18}	137^o	40^o	277^o	15 km	
This study [a]	?????	3.1×10^{18}	136^o	43^o	273^o	4 km	42[d]

[a]from P– and SH–waveform modelling.
[b]Hypocentre from USGS-PDE, projected up-dip to surface.
[c]Solution derived from P–waveforms only.
[d]P–waveforms (21) and SH–waveforms (21) used to derive solution.

Table 2. Details of ERS data used in this study. All SAR data copyright ESA.

	Date 1	Orbit 1	Date 2	Orbit 2	h_a	$B_\perp$ [†]
A) Change Detection	13/08/95	21323(ERS-1)	01/01/96	3654(ERS-2)	1165m.	8m.
B) DEM Generation	22/10/95	2652(ERS-2)	23/10/96	22325(ERS-1)	81m.	116m.

[†]$B_\perp$ is the perpendicular baseline separation of the satellite orbits;
$h_a \simeq 9416/B_\perp$

Table 3. Source parameters of the 1 October 1995 Dinar Earthquake from inversion of SAR data.

	Scarp Lat,Lon	Length	M_0 / N m	Slip	Strike	Dip	Rake	Depth
Seismic [a]	??? [b]	—	3.1×10^{18}	—	136^o	43^o	273^o	4 km[c]
Geodetic - 1 fault	38.110^o, 30.133^o	11.6 km	3.18×10^{18}	1.08 m	133^o	52^o	289^o	0.9 km – 7.0 km
Geodetic - 4 faults								
1 Main NW	38.134^o, 30.101^o	3.79 km	0.98×10^{18}	1.25 m	133^o	49.9^o	275^o	1.0 km – 5.9 km
2 Main Centre	38.110^o, 30.133^o	"	1.03×10^{18}	"	"	"	"	1.7 km – 6.8 km
3 Main SE	38.086^o, 30.165^o	"	0.69×10^{18}	"	"	"	"	3.5 km – 6.9 km
4 NW Continuation	38.158^o, 30.068^o	"	1.21×10^{18}	0.73 m	"	"	"	5.1 km – 15.5 km
			3.91×10^{18}					

[a]From P– and SH–waveform modelling [This Study].
[b]Centroid Location, projected up-dip to surface.
[c]Depth to Centroid.

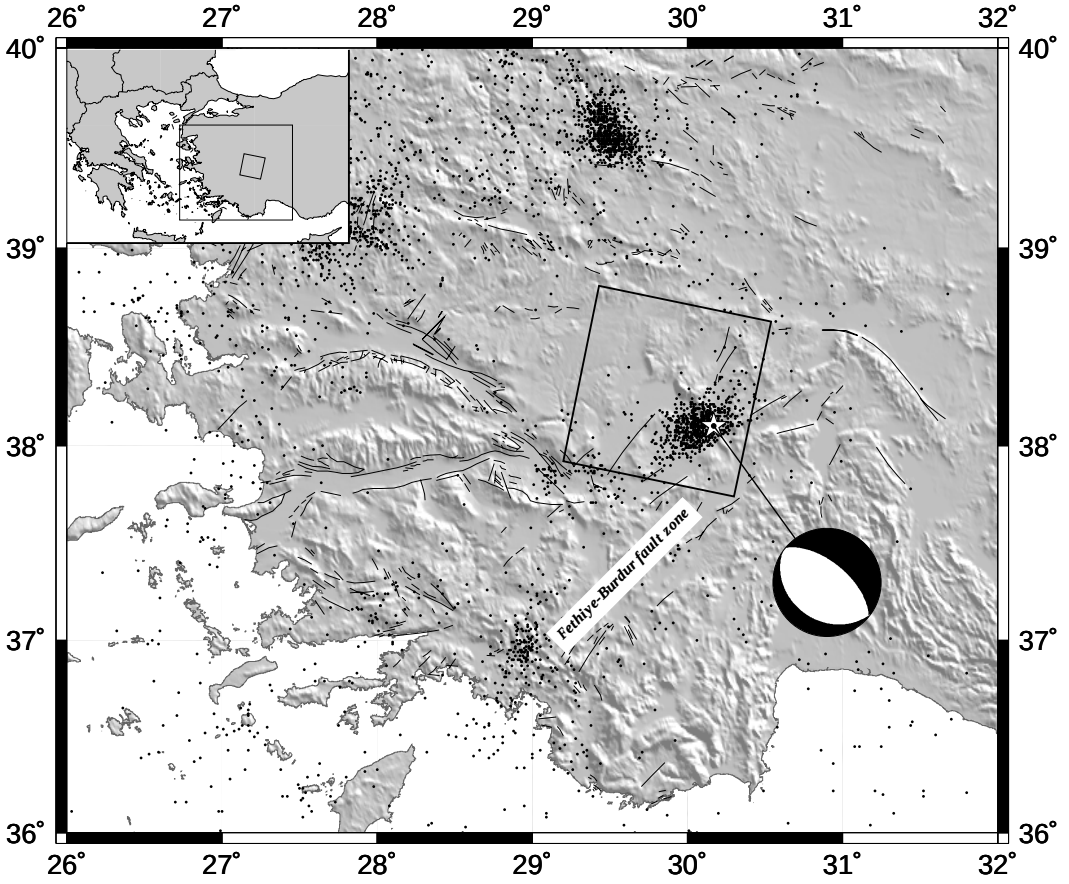

Fig. 1. Location of the 1 October 1995 Dinar earthquake [*Harvard CMT solution*] superimposed on a regional shaded relief map generated from GLOBE 1km topography database *[http://www.ngdc.noaa.gov/seg/topo/globe.shtml]*. The inclined box shows the nominal footprint of ERS SAR data used in this study (*track 293, frame 2835*). Also shown are the major faults of the region [14] and all recorded seismic activity from the ISC catalogue for January 1995 – March 1996.

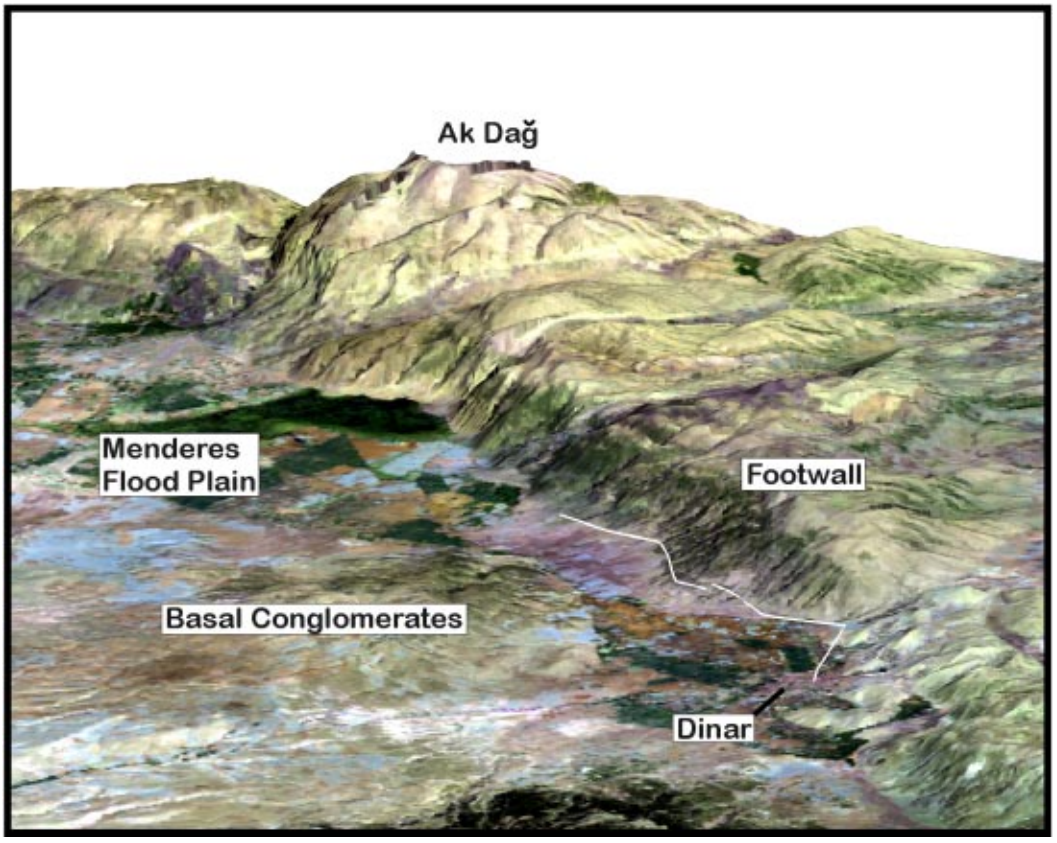

Fig. 2. Simulated 3D view looking SE along the Dinar fault, generated by draping Landsat TM data (bands 753 as rgb) over the high resolution DEM of the area generated in this study. The trace of the mapped surface rupture (white line) and the location of Dinar are shown [6]. Coherence in the interferogram is strongly correlated to surface type with high coherence over the basal conglomerates but low coherence over the agricultural flood plain of the Menederes river.

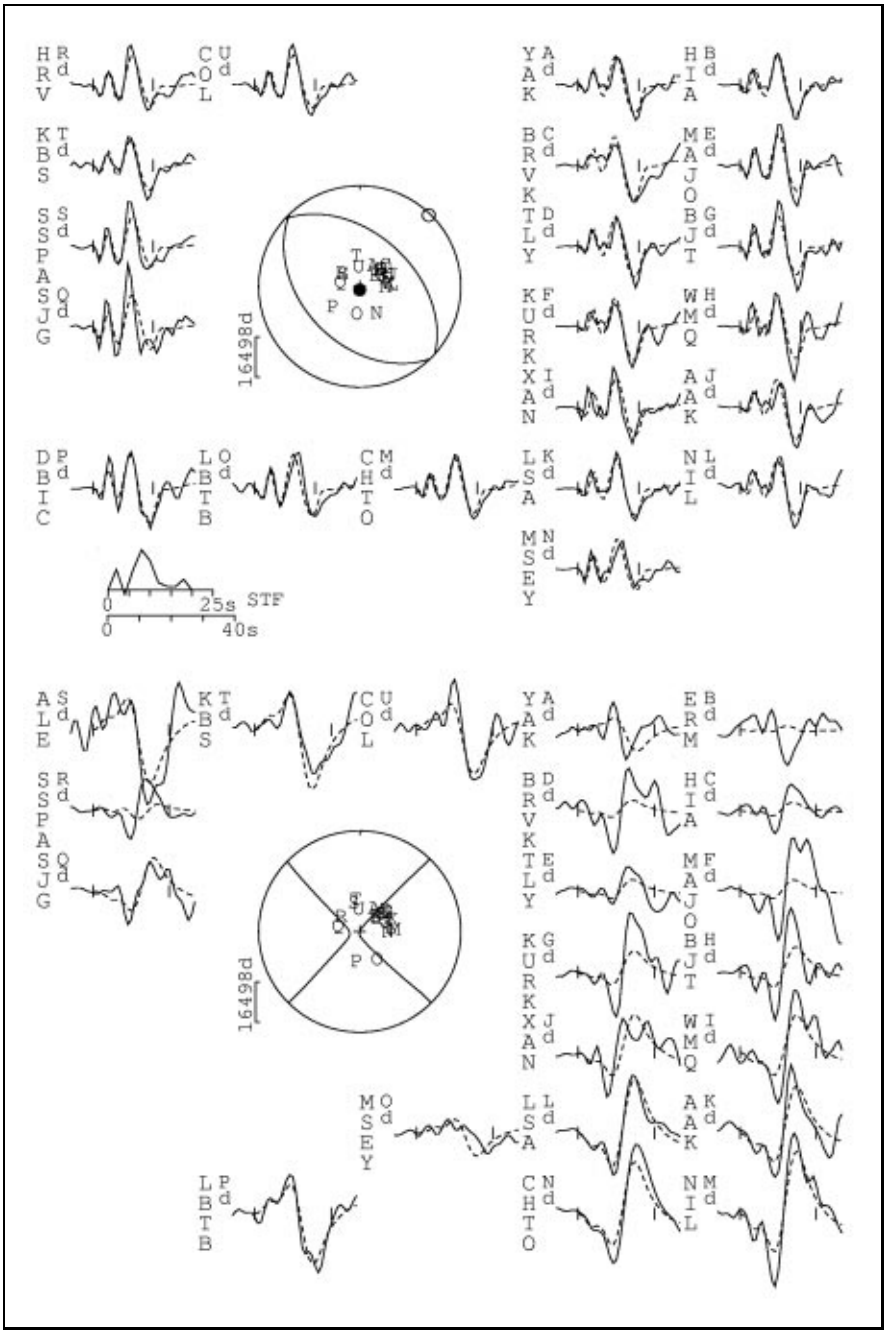

Fig. 3. P (top) and SH (bottom) observed (solid) and best-fitting synthetic (dashed) waveforms and focal spheres for the 1 October 1995 Dinar earthquake. Station positions on the focal spheres are identified by capital letters with waveforms arranged according to their location on the focal sphere. STF is the source time functon. Vertical ticks on the seismograms indicate the inversion window.

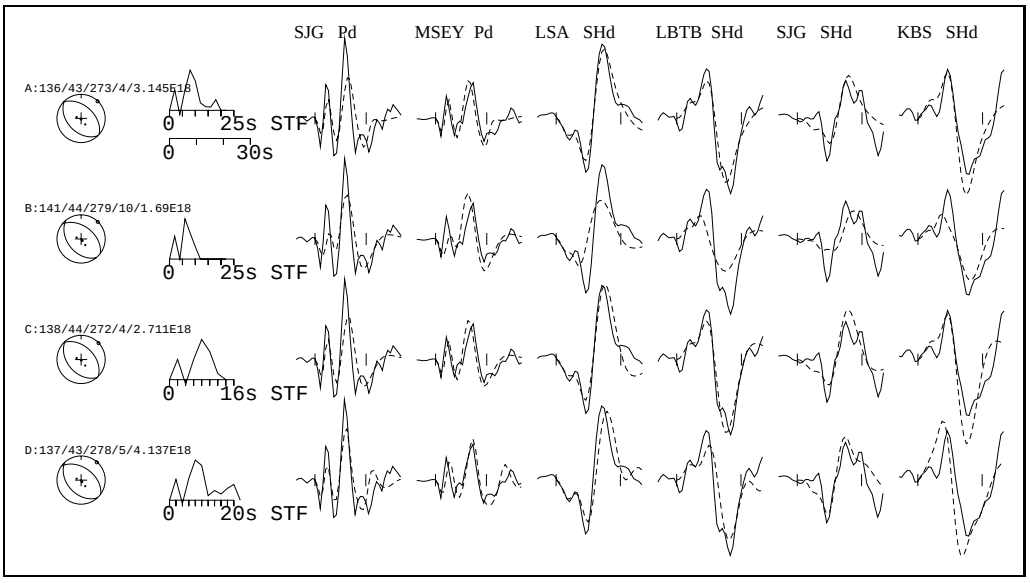

Fig. 4. Real (solid) and synthetic (dashed) waveforms recorded at 6 different locations on the focal sphere. Vertical dashes indicate the length of the inversion window. A) Best fitting solution; B) Solution with depth constrained to 10 km; C) Solution with source time function limited to 14 seconds duration; D) Solution with source propagating NW (315^o) at 2 km s^{-1}

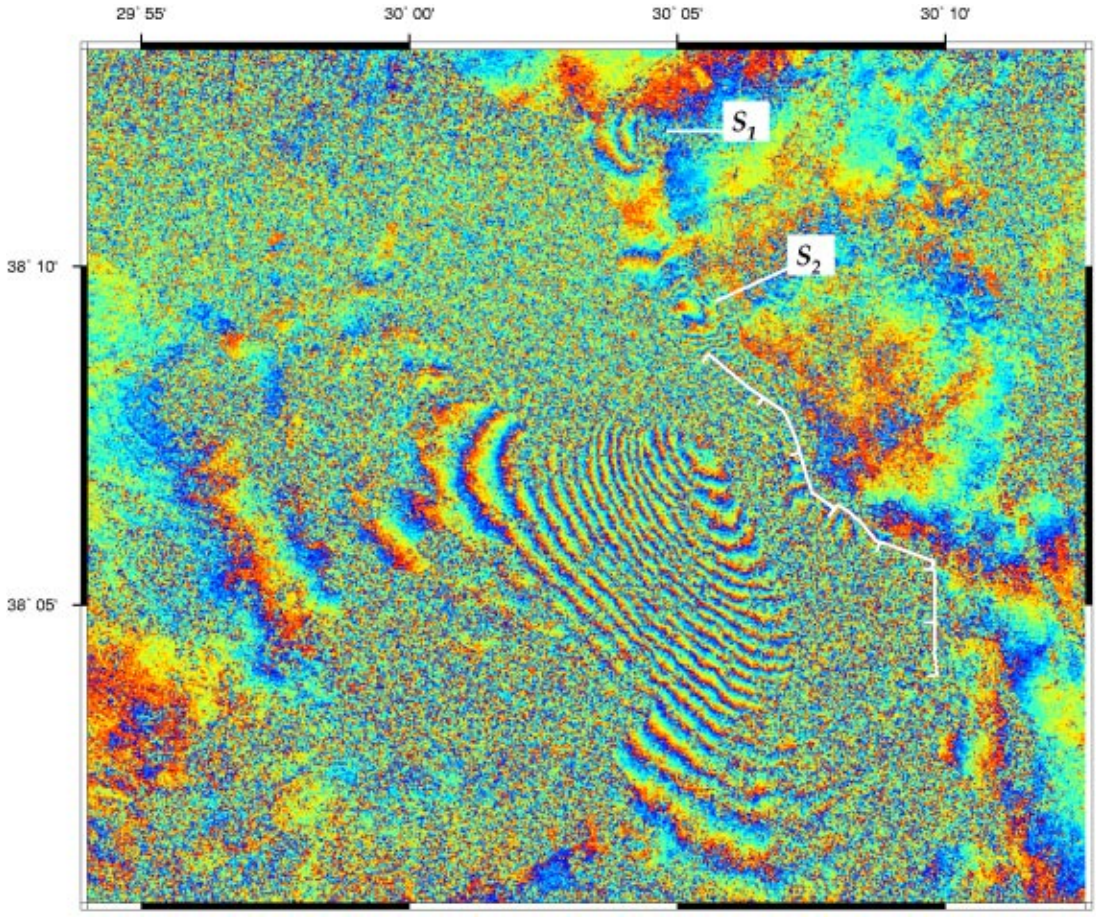

Fig. 5. Interferogram for the Dinar Earthquake showing the location of the surface rupture (white line). The interferogram has been corrected for topographic contribution using a DEM derived from a SAR tandem pair. S_1 and S_2 denote the location of localised, high gradient residual fringes, probably the result of small local land slips.

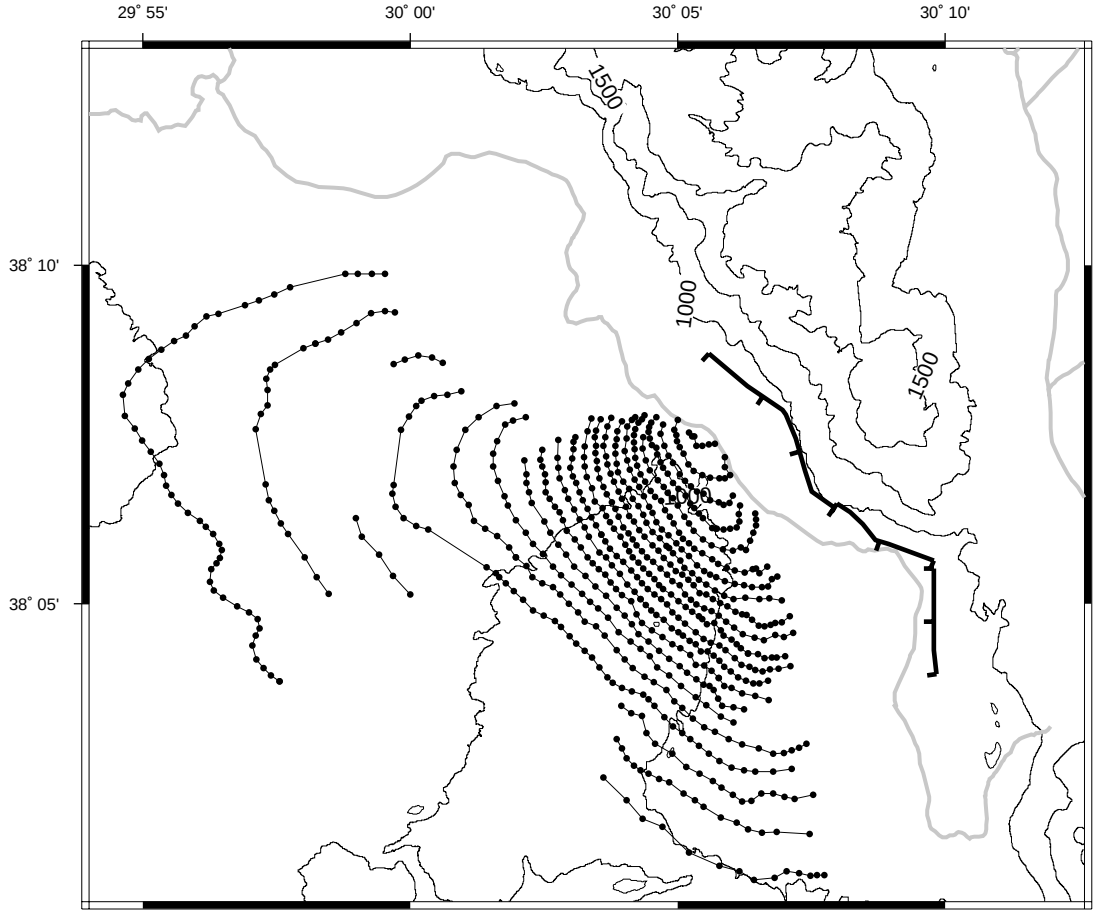

Fig. 6. Location of digitised fringe boundaries, where phase = 0 or 2π, used to constrain interferometric inversion. Discreet points are represented by black circles with black lines joining points of equal phase. Also shown are topographic contours at 250 m intervals from the digital elevation model derived in this study, the location of the Menderes river (grey line) which flows to the NW at the base of the fault footwall, and the mapped surface rupture (thick black line).

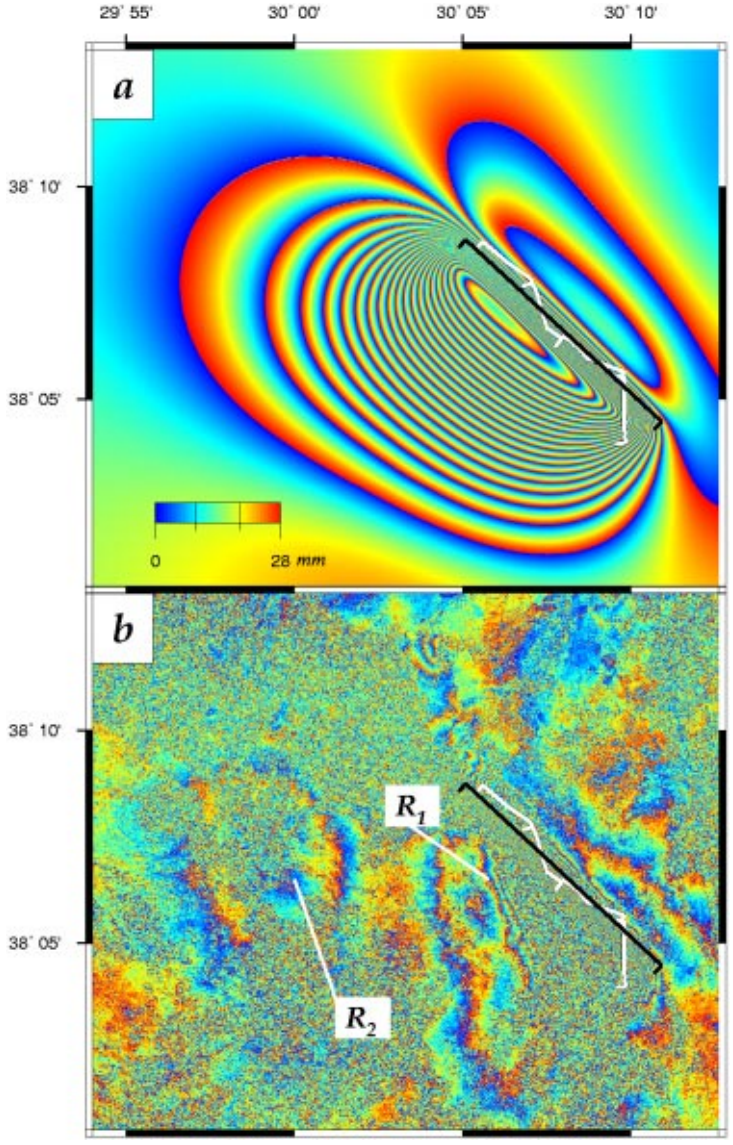

Fig. 7. a) Model Interferogram using a best fit single fault model showing the location of the mapped surface rupture (white line) and the model fault plane (black line) b) Residual interferogram, the result of subtracting the model interferogram from the real interferogram. R_1 and R_2 denote the location of the largest residuals using this model.

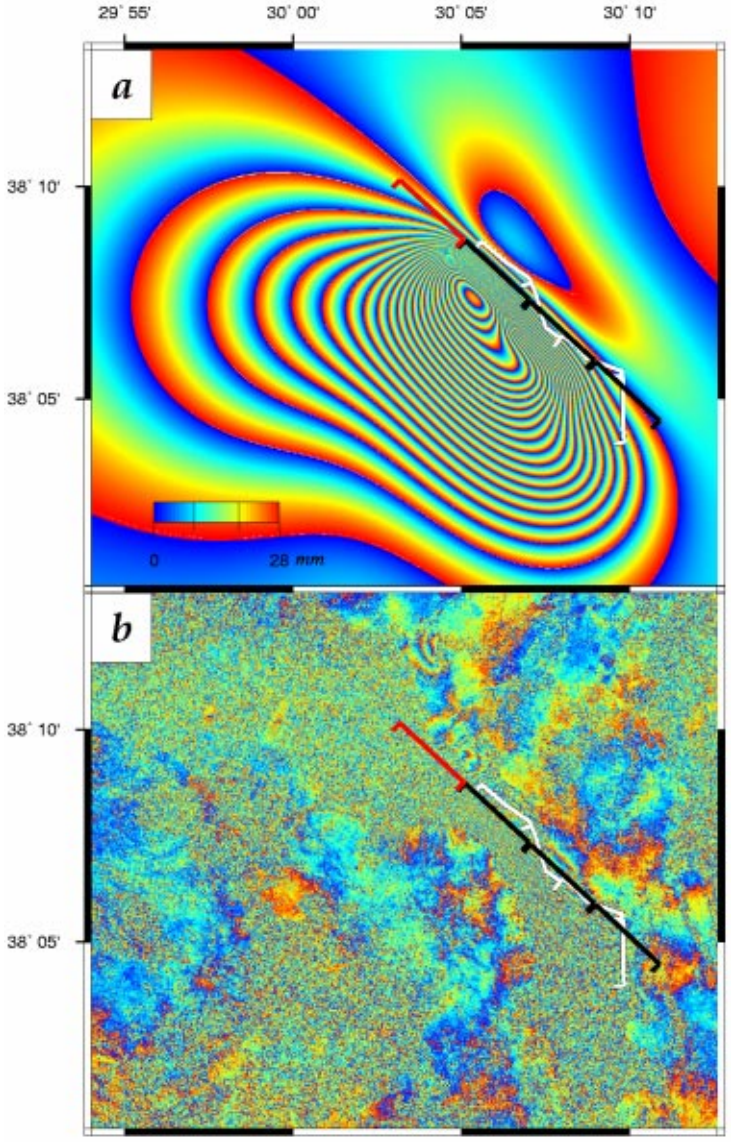

Fig. 8. a) Model Interferogram using a best fit model,comprising three segments along the main ruture (black lines) and a deeper extension to the NW (red line). The location of the mapped surface rupture (white line) is shown for reference b) Residual interferogram, the result of subtracting the model interferogram from the real interferogram.

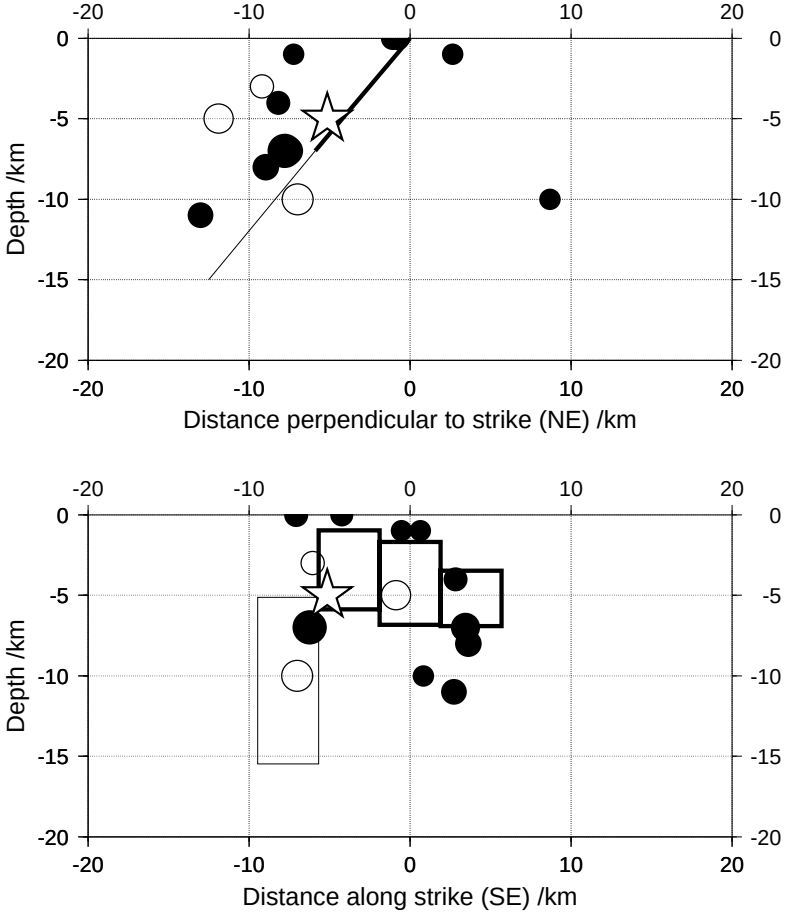

Fig. 9. Foreshock (open circles) and aftershock (closed circles) activity (KOERI Network, $M_d >= 4$) between 13/08/95 and 1/1/96 projected perpendicular to and along strike. All activity is within two weeks of the mainshock. The radius of the circles varies proportionally to M_d with the largest event being 4.9 and the smallest 4. The location of our geodetic model fault planes are shown and a star indicates the mainshock location.